

## Parameter identification of a jet pipe electro-pneumatic servo actuator

Shawki Al-Saloum, Ali Taha  and Ibrahim Chouaib 

Department of Electronic and Mechanical Systems, Higher Institute for Applied Sciences and Technology (HIAST), Damascus, Syria

### ABSTRACT

This paper presents experimental parameter identification of a jet pipe electro-pneumatic servo actuator model, which represents a class of high performance fast actuation systems. Parameter identification is given including detailed representation of linear dynamics, hysteresis, and the mass flow rate characteristics of the jet pipe servo valve, besides the static friction model of the linear pneumatic cylinder. Model parameters are identified and the model formulation is validated through simulation and experimentation. The main contribution of this work is threefold. Firstly, the mass flow rate characteristics are identified using the pressure dynamic equation in one cylinder chamber without the use of a flow sensor. Secondly, a lag behaviour related to the non-modelled dynamics is found out by performing an experimental identification of the frequency response of the servo valve. Thirdly, a new experimental setup is presented to give the static friction model as a function of not only the relative velocity but also the pressures in the two cylinder chambers. The agreement between simulations and experimental data indicates that the Parameter identification methods presented are valid and constitute valuable tools, whether in the analysis and the design of actuation systems, or for use in model-based control. The modelling methodology used in this paper can be generalised to similar electro-pneumatic servo actuators.

### ARTICLE HISTORY

Received 28 May 2015  
Accepted 10 August 2016

### KEYWORDS

Pneumatic cylinder; jet pipe servo valve; mass flow rate; static friction model

## 1. Introduction

Electro-pneumatic servo actuators are commonly used in various applications, especially in positioning, because they have many advantages like low cost, lightness, durability and cleanness when compared with the hydraulic actuators. Also because of self-cooling properties, easy maintenance, good power to weight ratio, fast acting with high accelerations, and installation flexibility, besides the compressed air is available in all industrial plants. On the other hand, pneumatic actuation systems have some undesirable characteristics which limit their use in some applications that require big forces and torques. These undesirable characteristics derive from the high compressibility of the air and from the nonlinearities presence in pneumatic systems, such as the nonlinear mass flow rate characteristics, dead zone, and hysteresis in the servo valve, besides the friction in the linear pneumatic cylinder.

The jet pipe electro-pneumatic servo actuator consists of a jet pipe electro-pneumatic servo valve and a linear pneumatic cylinder. The main advantages of the jet pipe electro-pneumatic servo valve are: no dead zone nonlinearity and good linear behaviour of electro-mechanical part, besides miniature size, short dynamic response time due to low inertia, high magnetic stiffness, and high reliability due to simple construction (Toorani *et al.* 2010).

Electro-pneumatic servo actuators have been studied in literature. An analytical and experimental investigation of a jet pipe electro-pneumatic servo actuator designed for use in the Utah/MIT dexterous hand has been performed by Henri *et al.* (1998). The nonlinear model, the nonlinear affine model, and the linear tangent model of electro-pneumatic servo actuator have been presented by Brun (1999) and Girin (2007) which have been used for simulation and controller design purposes. A nonlinear mathematical model of pneumatic servo actuators with a new equation for valve flow rate has been addressed by Valdiero *et al.* (2011). Modelling and controlling of pneumatic actuator driven by proportional servo valves have been presented by Le (2011).

This paper is organised as follows: in Section 2, parameter identification of the jet pipe electro-pneumatic servo valve will be obtained. In Section 3, the model of the two cylinder chambers represented by the rate of change of the pressure inside each chamber will be presented. In Section 4, the mechanical equations including friction model will be given. In Section 5, the final nonlinear model of the jet pipe electro-pneumatic servo actuator will be offered. Finally, the experimental validation of the final nonlinear model will be presented in Section 6.

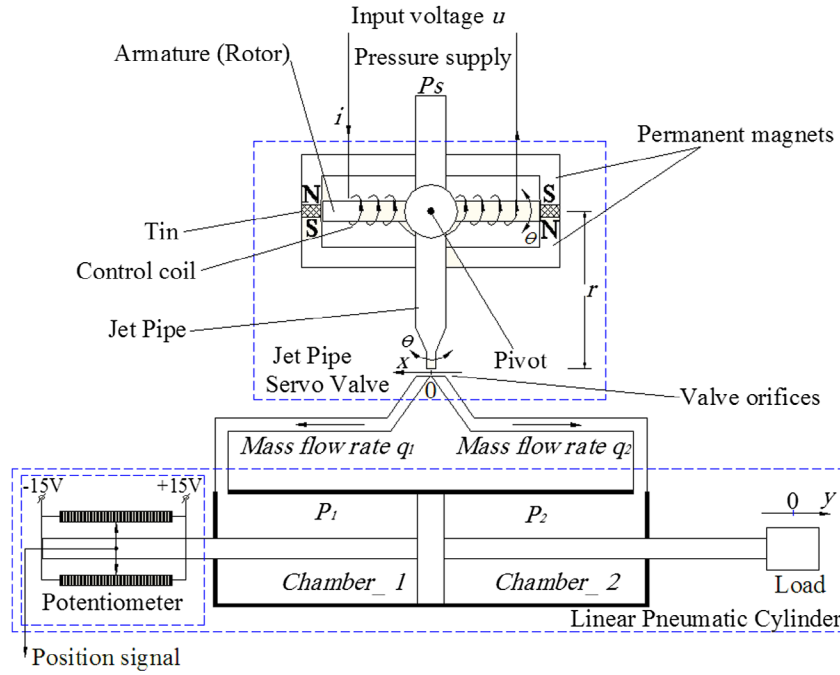


Figure 1. The jet pipe electro-pneumatic servo actuator.

## 2. Parameter identification of the jet pipe electro-pneumatic servo valve

The single-stage open loop jet pipe servo valve, in-house developed, consists of a small diameter aluminium tube, which directs a high pressure air flow toward the orifices to each side of the pneumatic cylinder, fixed at one end with the rotor of a limited angle torque motor as shown in Figure 1. The armature (rotor) can rotate with small angle ( $\pm 0.05236$  [rad] =  $\pm 3$  [°]) inside two parallel control coils and between a couple of permanent magnets separated by a magnetic insulator material (tin). The two magnets tend to keep the armature in a null position ( $\theta = 0$ ), for zero input voltage, the magnetic flux density in the four air-gaps is equal. That causes magnetic balance in the four air-gaps. By connecting an input voltage that can supply a current to the control coils, an unbalance of flux density in the air-gaps is produced, which results in a new equilibrium of rotor position. Inherently, the high stiffness of the magnet makes it like a spring with a stiffness torque proportional to the angular position, and the torque produced by the flux of the control coil is proportional to the current.

### 2.1. Linear dynamic characteristics

The linear dynamic characteristics of the jet pipe electro-pneumatic servo valve system are based on the dynamic equations of the motor that are described by the differential Equation (1), besides the geometric Equation (2).

$$\begin{cases} u - \left( \frac{\partial \theta(i, \theta)}{\partial \theta} \right) \frac{d\theta}{dt} - \left( \frac{\partial \theta(i, \theta)}{\partial i} \right) \frac{di}{dt} - Ri = 0 \\ T_m = J \frac{d^2 \theta}{dt^2} + K_f \frac{d\theta}{dt} + T_s(\theta) \end{cases} \quad (1)$$

$$x = r\theta \quad (2)$$

Here, the flux linkage  $\theta(i, \theta)$  is a nonlinear function of the current  $i$  and the angular position  $\theta$ . The variables:  $T_m$ ,  $T_s$  and  $K_f$  denote the motor developed torque, the stiffness torque, and the frictional coefficient, respectively. The jet pipe length and the jet pipe linear position are denoted by  $r$  and  $x$ , respectively.  $J$  is the moment of inertia of the bundle of rotor and jet pipe. Because of the small range of operation of  $\theta(\pm 0.05236$  [rad] =  $\pm 3$  [°]), it can be assumed that  $T_m$  is directly proportional to the current, the stiffness torque  $T_s$  is directly proportional to angular position  $\theta$ , and the differential  $\partial \theta(i, \theta) / \partial \theta$  term is approximately constant. If the other differential term  $\partial \theta(i, \theta) / \partial i$  is approximated to a constant value, then the Equations (2) and (3) can define an acceptable linear model.

$$\begin{cases} u - K_b \frac{d\theta}{dt} - L \frac{di}{dt} - Ri = 0 \\ T_m = J \frac{d^2 \theta}{dt^2} + K_f \frac{d\theta}{dt} + T_s(\theta) \end{cases} \quad (3)$$

where  $T_m = K_t i$ ,  $T_s = K_s \theta$ ,  $L$  is control coil inductance,  $R$  is control coil resistance, and  $K_b$  is back electro motive force constant. By simple mathematical manipulation of the Equations (2) and (3), a third order transfer function can be given as follows with  $s$  is the Laplace-domain variable:

$$\begin{aligned} G_{jp}(s) &= \frac{X(s)}{U(s)} \\ &= \frac{\frac{rK_t}{JL}}{s^3 + \left( \frac{K_f}{J} + \frac{R}{L} \right) s^2 + \left( \frac{RK_f + K_b K_t + K_s L}{JL} \right) s + \left( \frac{RK_s}{JL} \right)} \quad [\text{m/V}] \end{aligned} \quad (4)$$

**Table 1.** Parameters values of the third order transfer function.

Torque motor constant $K_t$ [Nm/A]	2.4
Back electro motive force constant $K_b$ [Vs/rad]	0.1
Control coil resistance $R$ [ $\Omega$ ]	193
Control coil inductance $L$ [mH]	16
Rotor moment of inertia $J$ [kg m <sup>2</sup> ]	$6.8 \times 10^{-6}$
Frictional coefficient $K_f$ [Nms/rad]	$6 \times 10^{-5}$
Magnetic stiffness constant $K_s$ [Nm/rad]	0.8
Jet pipe length $r$ [mm]	22.5

$J$  can be easily calculated based on the geometry and the materials of the rotating parts.  $r$ ,  $R$ ,  $L$ ,  $K_p$ , and  $K_s$  can be easily measured in the same way suggested by Toorani *et al.* (2010). The difficulty is in estimating  $K_f$  and  $K_b$ . This problem has been solved by taking advantage of the two following methods during model validation of the servo valve in Section 2.4:

- $K_b$  affects the value of resonance frequency in frequency response of the servo valve, so the value of  $K_b$  will be tuned such that the resonance frequency of the model is identical to the real resonance frequency.
- $K_f$  affects the amplitude at resonance frequency in the frequency response of the servo valve, so the value of  $K_f$  will be tuned such that the amplitude at the resonance frequency of the model is identical to the real amplitude at real resonance frequency of the servo valve.

All the parameters of the third order transfer function (4) will be shown after the model validation of the servo valve in Section 2.4 (Table 1).

**Remark 1.** The resonance frequency  $f_r$  of the jet pipe servo valve has been easily measured using frequency generator and vibration sensor (In our case:  $f_r \approx 49$  [Hz]).

## 2.2. Hysteresis identification

There is a significant amount of hysteresis in jet pipe position vs. input voltage relationship that has an adverse effect on the actuator performance. This hysteresis can be identified by incrementally ramping the input voltage up and down until the position saturation of the jet pipe ( $\pm 1$  [mm]). The characteristic of major hysteresis loop has been obtained as depicted in Figure 2. The maximum separation between the halves of the major hysteresis loop is about 0.5 [V]. Therefore, comparing the maximum distance between the midpoints lines and the major loop 0.25 [V] to the input voltage operation range 6 [V], gives maximum hysteresis of approximately 4%. So, hysteresis nonlinearity can be represented by midpoints lines as noted by Henri *et al.* (1998), which yield the Equation (5).

$$u = \begin{cases} -2.9x - 0.03 & [V] \text{ for } |x| \leq 0.46 \text{ [mm]} \\ -1.674(x - 0.84) - 2 & [V] \text{ for } 0.46 \text{ [mm]} \leq x \leq 0.84 \text{ [mm]} \\ -5(x - 1) - 2.8 & [V] \text{ for } 0.84 \text{ [mm]} \leq x \leq 1 \text{ [mm]} \\ -1.3(x + 0.46) + 1.296 & [V] \text{ for } -0.76 \text{ [mm]} \leq x \leq -0.46 \text{ [mm]} \\ -5.475(x + 1) + 3 & [V] \text{ for } -1 \text{ [mm]} \leq x \leq -0.76 \text{ [mm]} \end{cases} \quad (5)$$

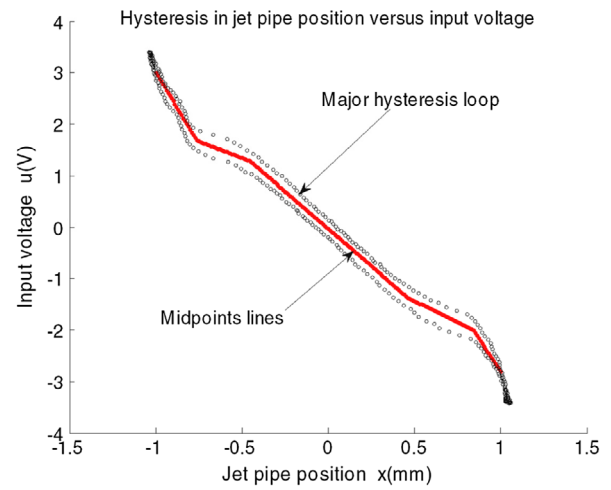


**Figure 2.** Hysteresis in jet pipe position vs. input voltage and the midpoints lines.

## 2.3. Mass flow rate characteristics

The mass flow rate characteristics are a key part of the servo valve. The identification method of mass flow rate characteristics is based on a systematic series of experiments that have been performed on the test setup of Figure 3, in order to determine the mass flow rate through the orifices of the valve as a function of the valve's control signal  $u$  (which is proportional to orifice area), and actuator chamber's pressure  $p$ . The experiments are performed with a constant supply pressure  $p_s = 10$  [bar], constant external pressure  $p_{\text{Atm}} = 1$  [bar], and constant chamber\_1 volume. The constant volume is measured by the potentiometer integrated with the piston rod and the measured dead volume; the ambient temperature remains constant at  $T = 298.15^\circ$  [K] due to air cooling system. The variation of the air source temperature (compressed-air tank to 80 [bar]) and the leakage in the cylinder are neglected. The pressure sensor range is 10 [bar], the accuracy is 0.05% FS, and 1 [KHz] bandwidth (from EFE). Temperature is measured with an exposed type K thermocouple with accuracy  $1^\circ$  [K].

**Remark 2.** Since the valve orifices 1 and 2 have identical mechanical structures, the pressure  $p_1$  and  $p_2$  are considered symmetric with respect to the control voltage. So, using only the chamber\_1 for modelling is sufficient as noted by Le (2011).

In each experiment, charging process (for control input  $|u|$ ) and discharging process (for control input  $-|u|$ ) of chamber\_1 with a constant volume have been performed. The pressure variation in chamber\_1 that is being charged or discharged is measured in real time with sampling

time  $t_s = 1$  [ms]. This was carried out for control voltage values:  $|u| = \{0, 0.29, 0.57, 1.15, 1.73, 2.29, 2.86, 3.4\}$  [V]

During charging and discharging, the air inside the actuator chamber can be treated as undergoing a poly-tropic process with poly-tropic index ( $n$ ), and the term  $n/(n - 1)$  represents the slope of the relationship between  $\ln(p)$  and  $\ln(T)$  as cited by Thorncroft (2007). By setting the pressure and temperature sensors inside the cylinder chamber, a major charging and discharging test with maximum input voltage ( $|u| = 3.4$  [V]) is carried out with sampling time  $t_s = 10$  [ms]. Consequently,

the variation of poly-tropic index in the actuator chamber during charging and discharging is close to 1 in the majority of the charging and discharging processes as shown in Figures 4 and 5, besides the region where  $n = 0.72$  is not attainable in the real work of the electro-pneumatic actuator within the closed-loop control system because its settling time is less than 0.5 [s]. So, the process can be considered as an isothermal process with an acceptable error (less than 5%).

The mass flow rate is obtained by differentiating, with respect to time, the perfect gas law equation of state of

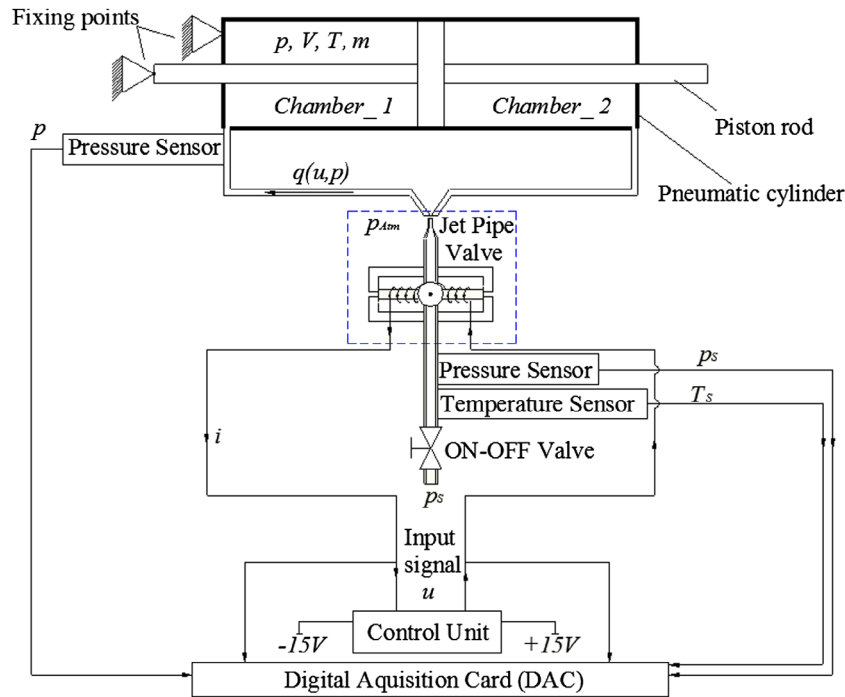


Figure 3. Test setup to determine the mass flow rate characteristics.

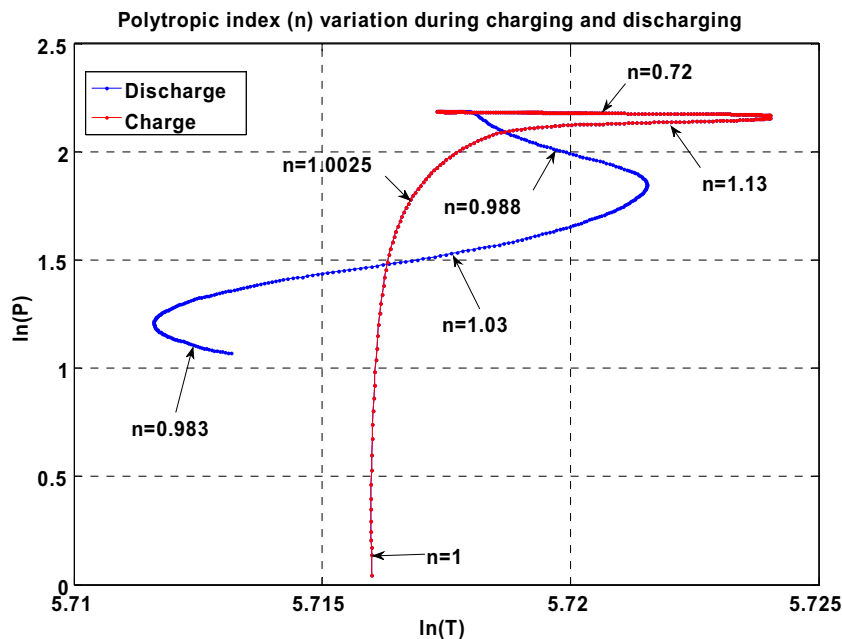


Figure 4. Polytropic index ( $n$ ) variation during major charging and discharging test with  $T$  in Kelvin and  $p$  in bar.

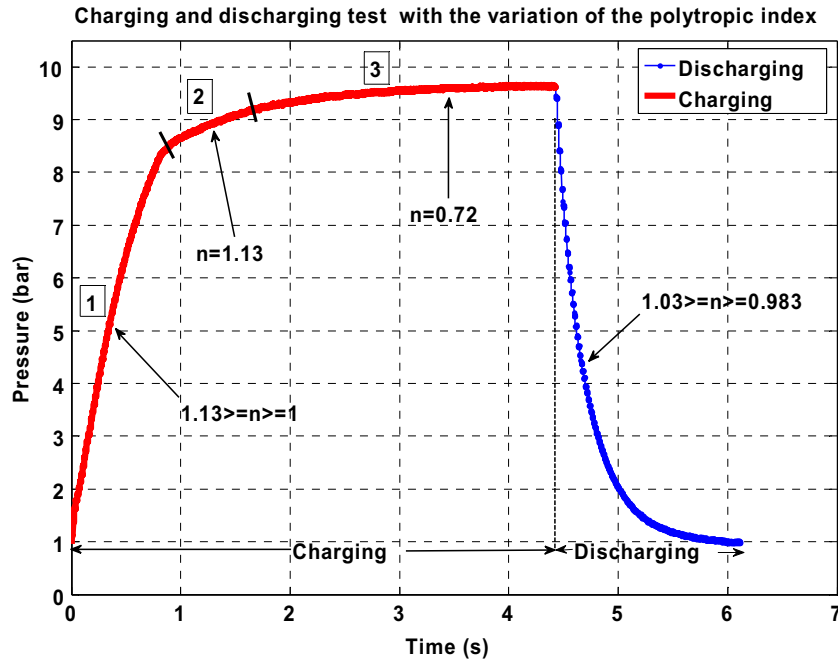


Figure 5. Major charging and discharging test with poly-tropic index ( $n$ ) variation.

the air contained in a known constant volume. The perfect gas law is given in Equation (6).

$$pV = mrT \quad (6)$$

where  $V$ ,  $r$  and  $T$  are constants ( $V$  is the volume of chamber\_1,  $T$  is the temperature of the air source, and  $r$  is the perfect gas (air) constant),  $p$  is the pressure in chamber\_1, and  $m$  is the mass of air in chamber\_1. Differentiating Equation (6) and rearranging it yields the Equation (7).

$$\dot{m} = q = \frac{V}{rT} \dot{p} \quad (7)$$

In practice, the differentiation of the experimental pressure signal gives bad signal because of the noise. So, to overcome this problem, one of the robust differentiator algorithms (adaptive super twist differentiator algorithm) via sliding mode technique is tuned and used off-line in order to estimate the derivation of the noisy pressure signal (Refer to Dridi (2011) for further details) and zero phase lag is assured.

In each charging and discharging experiment, the input voltage  $|u|$  is applied on the servo valve for 4.4 [s] (charging process); then the input voltage  $-|u|$  is applied on the servo valve for 1.8 [s] (discharging process). During these processes, the pressure vs. time data inside cylinder chamber is measured, and by applying Equation (7), the mass flow rate vs. time data is obtained. Consequently, the mass flow rate vs. pressure data (two curves) can be deduced as shown in Figure 6, and then the two curves of the mass flow rate vs. pressure are redrawn as function of input voltage and pressure as shown in Figure 7. The same procedure will be repeated for the other values of  $|u|$ .

The mass flow rate characteristics are obtained by fitting the experimental data (the curves of mass flow rate vs. input voltage and pressure for all values of  $|u|$ ) with a nonlinear fifth order function with a maximum absolute error about 0.0005 kg/s] which corresponds to a maximum relative error about 5%.

The mass flow rate characteristics as a nonlinear function of the input voltage and the chamber pressure is given by Equation (8) and shown in the Figure 7.

$$\begin{aligned} q(u, p) = & (3.562 + 1.233 u - 2.037 p + 0.1701 u^2 \\ & - 0.7901 up + 0.6697 p^2 + 0.1335 u^3 \\ & - 0.1801 u^2 p + 0.3379 up^2 - 0.1243 p^3 \\ & + 0.01195 u^4 - 0.01784 u^3 p + 0.03335 u^2 p^2 \\ & - 0.0413 up^3 + 0.008227 p^4 - 0.007284 u^5 \\ & - 0.0005998 u^4 p + 0.0003319 u^3 p^2 \\ & - 0.001838 u^2 p^3 + 0.001729 up^4 \\ & - 0.0001519 p^5)/1000 \text{ [kg/s]} \end{aligned} \quad (8)$$

#### 2.4. The nonlinear model

After obtaining and identifying the mass flow rate characteristics (8), the theoretical model of the jet pipe electro-pneumatic servo valve can be presented by the block diagram in Figure 8, where the third order transfer function is that one given in Equation (4), the hysteresis approximation by midpoints lines is described in Equation (5), and the mass flow rate characteristics are given in Equation (8). This theoretical model must be validated by comparing the frequency response of the theoretical model with the frequency response of the servo valve (the real system). Here, the intended frequency response relates the input voltage in [V] to the

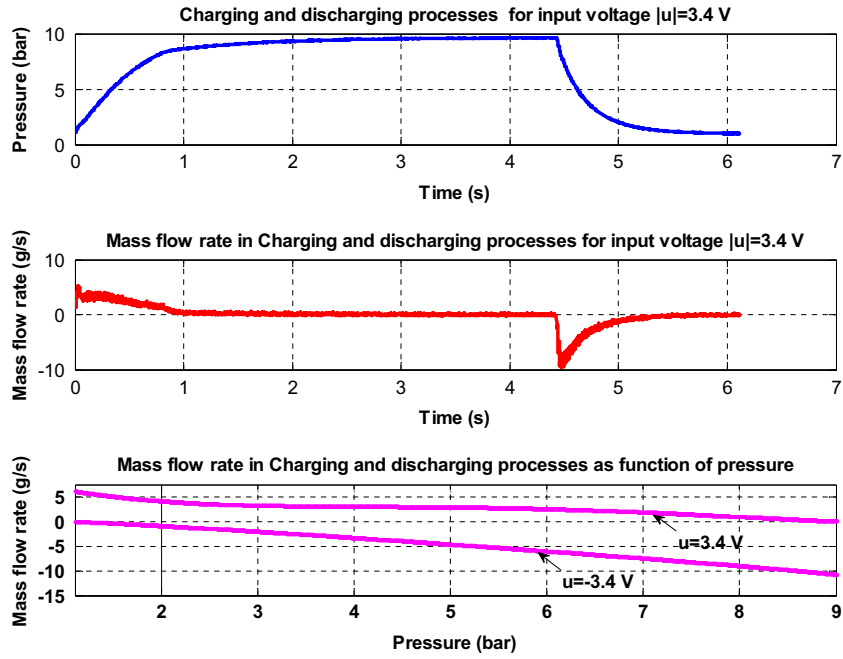


Figure 6. Identification of mass flow rate as a function of chamber pressure in charging with input voltage  $|u| = 3.4[V]$  and in discharging with input voltage  $-|u| = -3.4[V]$ .

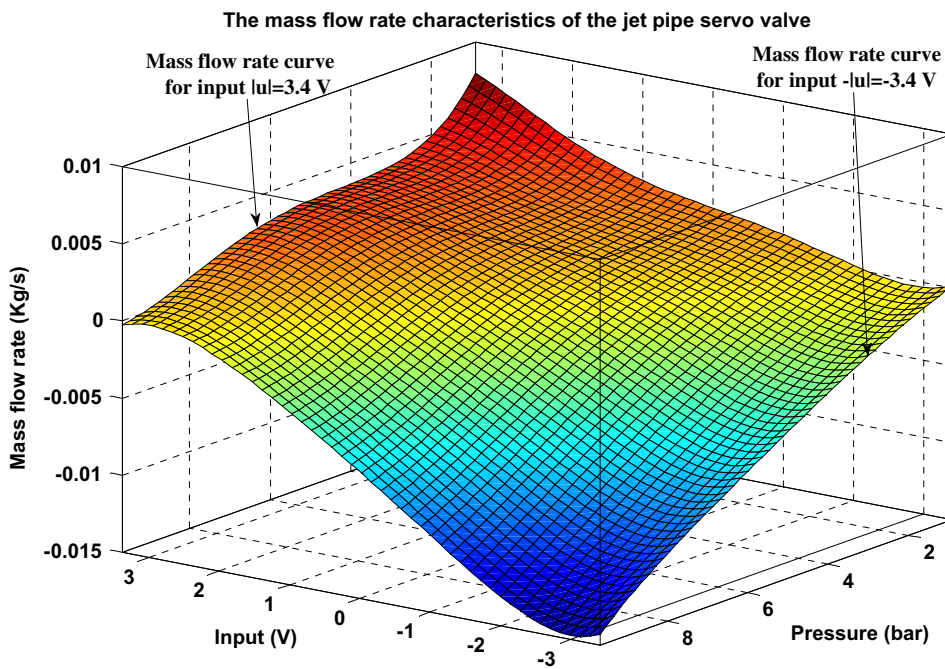


Figure 7. The mass flow rate characteristics of the jet pipe electro-pneumatic servo valve.

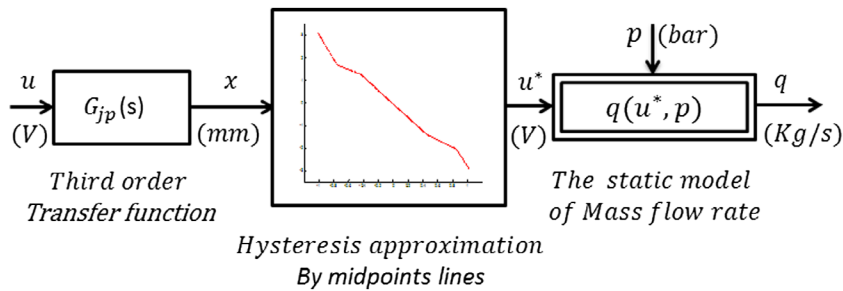


Figure 8. The theoretical model of the jet pipe electro-pneumatic servo valve.

mass flow rate in [kg/s]. The valve is fed by a flow of compressed air with a constant supply pressure  $p_s = 10$  [bar] and forced to move periodically by input sine wave with frequency range (1–70 [Hz]) and the output mass flow rate is obtained in the same way as mentioned in Section 2.3. The frequency response of the servo valve (the real system) shows extra delay and lag behaviours when compared with the theoretical model. The delay behaviour is about 2 [ms] which is associated with the electro-mechanical part as proved by Toorani *et al.* (2010), and the phase-lag behaviour that is modelled in Equation (9) is necessarily related to non-modelled dynamics as the mass flow rate dynamics, temperature error, pipe dynamic effect, differentiation, etc.

$$G_{Lag}(s) = \frac{1 + s/220}{1 + s/155} [V/V] \quad (9)$$

After tuning the parameters  $K_f$  and  $K_b$  in the same way as mentioned in Section 2.1, the characteristics of the third order transfer function (4) are shown in Table 1. Subsequently, the evaluation of the third order transfer function (4) according to Table 1 accompanied with the delay behaviour yields:

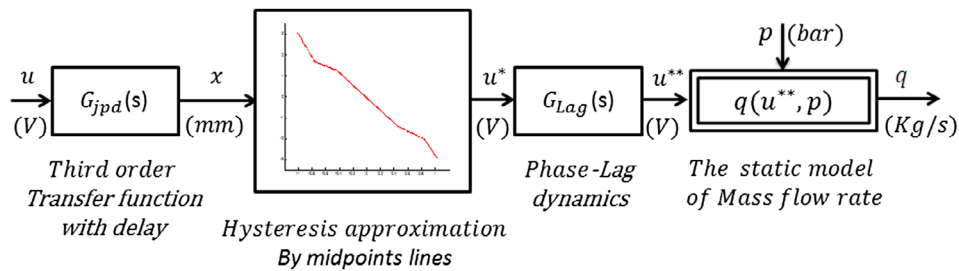


Figure 9. Nonlinear model of the jet pipe electro-pneumatic servo valve.

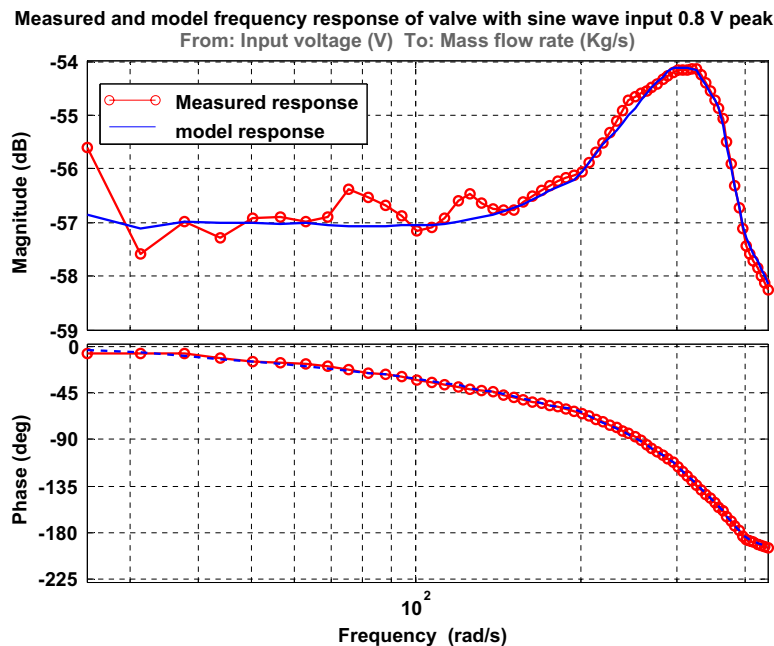


Figure 10. Measured and model frequency response of the servo valve with input 0.8 [V] peak.

$$G_{jpd}(s) = \frac{X(s)}{U(s)} \quad (10)$$

$$= \frac{4.96310^8 e^{-0.002s}}{s^3 + 1.207 \cdot 10^4 s^2 + 2.43 \cdot 10^6 s + 1.419 \cdot 10^9} [\text{mm}/\text{V}]$$

Thereafter, the final nonlinear model of jet pipe electro-pneumatic servo valve can be presented by the block diagram in Figure 9.

The frequency responses of the complete practical model and the real system are shown in Figures 10 and 11 for input amplitude 0.8 and 1.9 [V], respectively. A step response test confirmed the correctness of the modelling is shown in Figure 12. The servo valve is under damped with rise time of 6 [ms] and a 5% settling time of 36 [ms]. The hysteresis effect is clear in frequency responses (Figures 10 and 11). The hysteresis affect mainly the bode gain diagram and cause big error for small amplitude input signal at low frequencies, and this error becomes smaller in higher amplitude input signal and high frequencies.

### 3. Chamber model

Assuming air is a perfect gas undergoing an isothermal process, the rate of change of the pressure inside each

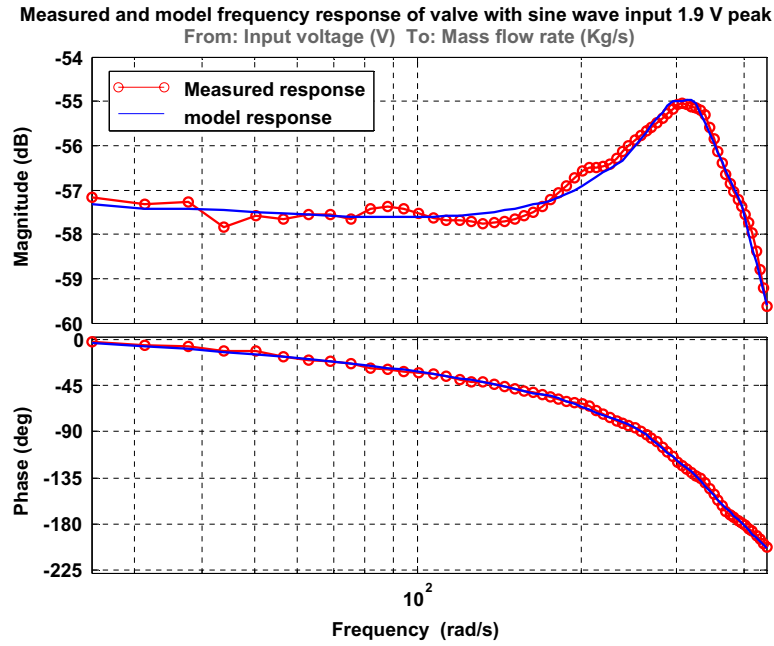


Figure 11. Measured and model frequency response of the servo valve with input 1.9 [V] peak.

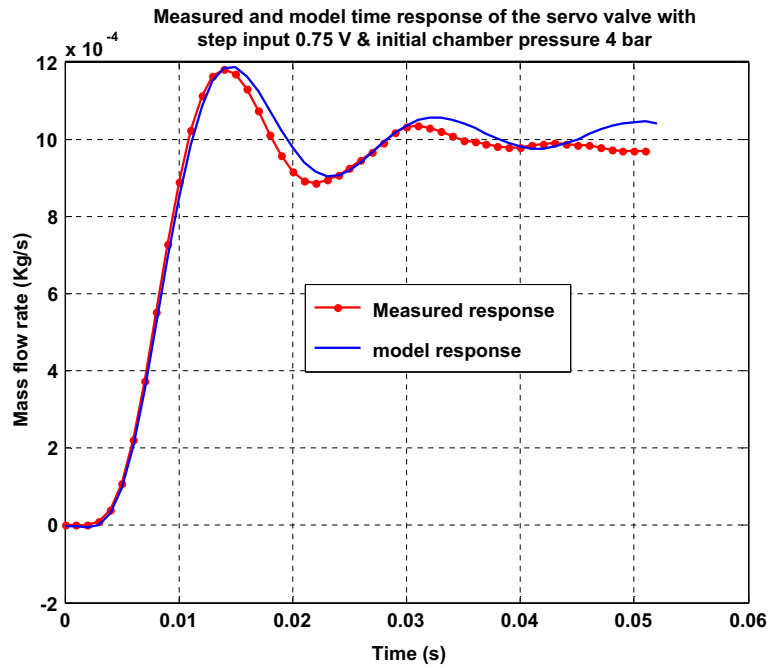


Figure 12. Measured and model time response with step input 0.75 [V] and initial chamber pressure 4 bar.

cylinder chamber can be expressed as in Equation (11) for the chamber in case of expanding and as in Equation (12) for the chamber in case of shrinking (refer to Girin (2007) for further details), knowing that  $u_1 = u = -u_2$  in our case, and  $T_1 = T_2 = T$  due to the isothermal process.

$$\frac{dp_1}{dt} = \frac{rT}{V_1(y)} \left( q(u, p_1) - \frac{S}{rT} p_1 v \right) \quad (11)$$

$$\frac{dp_2}{dt} = \frac{rT}{V_2(y)} \left( q(-u, p_2) + \frac{S}{rT} p_2 v \right) \quad (12)$$

where  $p$  is the pressure inside the chamber,  $q$  is the mass flow rates into or out of the chamber,  $r$  is the universal gas constant,  $T$  is the gas temperature,  $y$  is piston position,  $S$  is the effective piston area, and  $v$  is the piston velocity.  $V_1(y)$  And  $V_2(y)$  are chambers volumes as a function of piston position, which are given in our case as follows:

$$\begin{cases} V_1(y) = 0.005433y + 0.0001533 \text{ [m}^3\text{]} \\ V_2(y) = -0.005433y + 0.0001915 \text{ [m}^3\text{]} \end{cases} \quad (13)$$

## 4. Mechanical equations

### 4.1. Newton's second law

The model of the mechanical part is obtained by applying the fundamental principle of mechanics to the mobile part in translation. The balance of forces applied on the mass  $M$  of piston and its accessories is:

- The air forces in the actuator cylinder:  $S(p_1 - p_2)$ .
- The friction forces on the piston:  $F_f$ .

So, two state equations are obtained as follows:

$$\begin{cases} \frac{dy}{dt} = v \\ \frac{dv}{dt} = \frac{1}{M} [S(p_1 - p_2) - F_f] \end{cases} \quad (14)$$

### 4.2. Static friction model

The friction in the linear pneumatic cylinder arises mainly in the contacts of the piston and the rod seals with the cylinder walls; it has many diverse aspects that cause control problems such as static errors, limit cycles, and stick-slip, which limit the using of pneumatic cylinder in high precision positioning and low velocity tracking. Many models were developed to explain the friction phenomena. These models are based on experimental results rather than analytical deductions. The friction model which captures most of the friction behaviour in pre-sliding and sliding regimes is the LuGre friction model that is given by De Wit *et al.* (1995). When using the LuGre friction model, controller design becomes difficult because: (i) the friction parameters appear in a nonlinear fashion, and (ii) the system's internal state, which depends on unknown parameters, is not measurable. In this paper, the pneumatic cylinder is manufactured to work in sliding regime and supplied with a motion sensor that is not sensitive enough to sense the pre-sliding micro motions. So, Gaussian exponential static friction model, which can describe the friction phenomena of pneumatic cylinder in sliding regime, can be used in order to achieve precise position control and compensate friction in sliding regime, as cited by Ali *et al.* (2009), knowing that many experimental works have proved that a good static friction model in sliding regime can approximate the real friction force with a degree of confidentiality of 90%, as mentioned by Tijani Ismaila *et al.* (2011). The classic Gaussian model is represented by the friction force as a function of instantaneous sliding velocity, and it captures two basic frictions: Coulomb and viscous, besides the stribeck effect.

The general static friction model is (Refer to Serafin (2004)):

$$F_f = \begin{cases} F(v) & \text{if } v \neq 0 \\ F_e & \text{if } v = 0 \text{ and } |F_e| < F_s \\ F_s \cdot \text{sgn}(F_e) & \text{if } v = 0 \text{ and } |F_e| \geq F_s \end{cases} \quad (15)$$

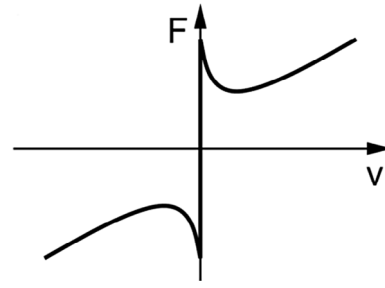


Figure 13. The static friction model.

where  $F_f$  is the friction force,  $v$  is the relative velocity,  $F_e$  is the external force,  $F(v)$  is an arbitrary function that looks like Figure 13, and  $F_s$  is the static (breakaway) force. A common form for the friction function  $F(v)$  is given by the following equation:

$$F(v) = F_C + (F_S - F_C) \cdot e^{-\left|\frac{v}{v_s}\right|^\delta} + F_v \cdot v \quad (16)$$

where  $F_C$  is Coulomb friction,  $F_v$  represents viscosity factor,  $v_s$  is called Stribeck velocity, and  $\delta$  is an empirical parameter. Refer to Ali *et al.* (2009),  $\delta = 2$  gives the Gaussian exponential static friction model as follows.

$$F(v) = F_C + (F_S - F_C) \cdot e^{-\left(\frac{v}{v_s}\right)^2} + F_v \cdot v \quad (17)$$

The frictional characteristics of pneumatic cylinder are mainly affected by guide seal rings, piston seal rings, and surface of cylinder bore (See Figure 14) and the pressure inside cylinder chambers as addressed by Heipl and Murrenhoff (2011). The pressures in cylinder chambers will change the stress state of the seal rings, and then the friction force will be different. When chamber pressure increases, the seal rings are pushed more firmly against the cylinder wall and the piston rod. So, the friction force will increase too. Evidently, the static friction model of the pneumatic cylinder depends not only on the piston rod relative velocity but also on the pressures in the two cylinder chambers. Subsequently, the Equation (17) must be changed to look like the following equation.

$$F(v, p_1, p_2) = F_C(p_1, p_2) + (F_S(p_1, p_2) - F_C(p_1, p_2)) \cdot e^{-\left(\frac{v}{v_s(p_1, p_2)}\right)^2} + F_v(p_1, p_2) \cdot v \quad (18)$$

The following task will be the identification of the static friction model parameters:  $F_C(p_1, p_2)$ ,  $F_S(p_1, p_2)$ ,  $v_s(p_1, p_2)$ , and  $F_v(p_1, p_2)$ .

#### 4.2.1. Experimental setup

To obtain the data for the parameter identification of the static friction model, a new experimental setup for measuring friction force in the pneumatic cylinder during sliding regime has been developed. The schematic diagram of the experimental setup is depicted in Figure 15. Where 1 is a hydraulic cylinder, 2 is a force sensor, 3 is the tested pneumatic cylinder which is

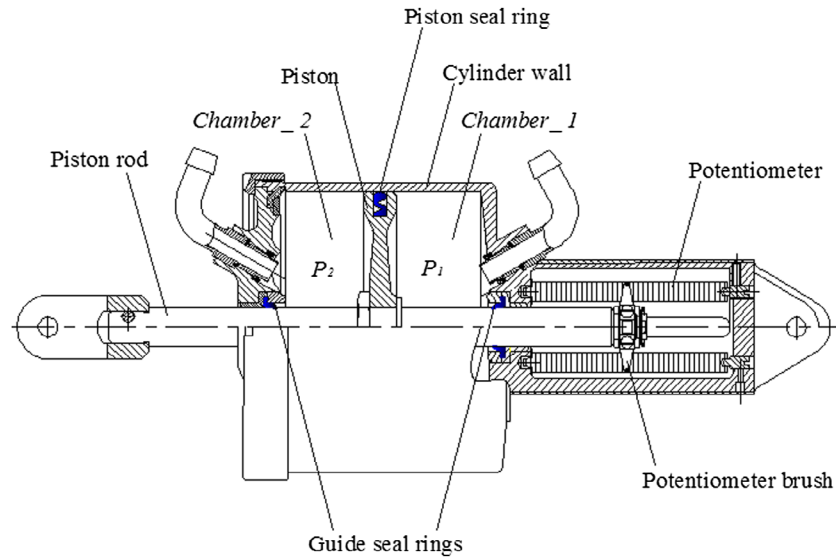


Figure 14. Piston and guide seal rings in the actual pneumatic cylinder.

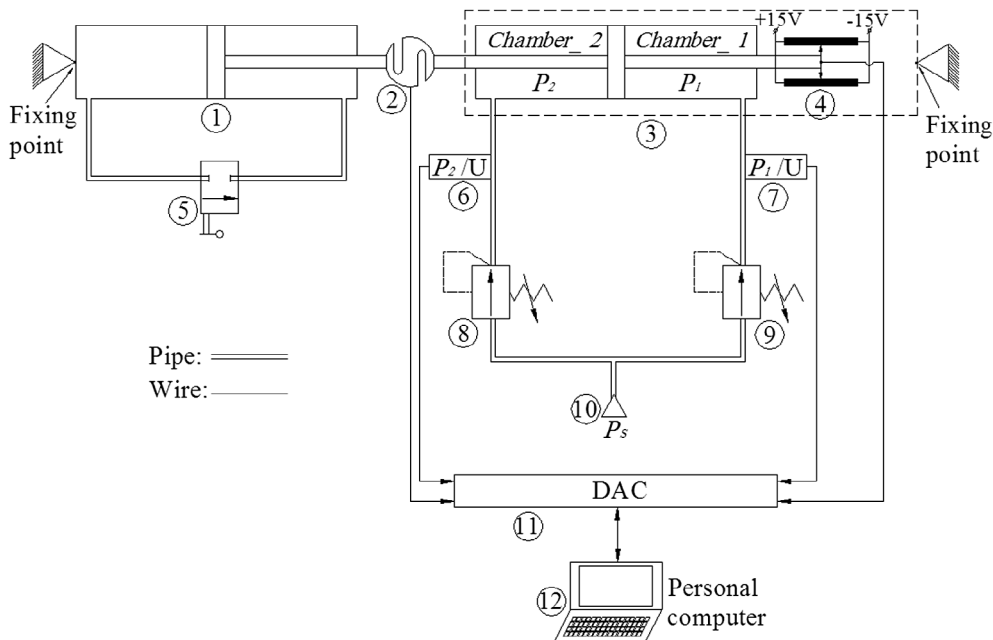


Figure 15. Schematic diagram of the experimental setup.

in-house manufactured, 4 is the displacement sensor, 5 is 2/2 way directional control valve with lever operated (shut-off valve), 6 and 7 are pressure sensors, 8 and 9 are pressure regulating valves, 10 is the pneumatic power source, 11 is the high-performance data acquisition card, and 12 is a personal computer. The motion of piston in the pneumatic cylinder is performed by self-pneumatic force resulted of the pressure difference between the two cylinder chambers. The closed hydraulic circuit is filled with hydraulic oil. It has two objectives.

The first objective is to stop the movement of the pneumatic cylinder's piston during the adjustment of the pressure in the two chambers when the shut-off valve is closed.

The second objective is to release the movement of pneumatic cylinder's piston from the rest when the shut-off valve is opened, and during this phase, the data acquisition card is used to record the data of the four sensors. The moving range of the hydraulic cylinder (0.1 [m]) is more than that one of the pneumatic cylinder (0.05 [m]), and the maximum load resulted of the closed hydraulic circuit when the shut-off valve is opened (350 [N] at piston velocity 0.6 [m/s]), which is less than the pneumatic force (550 [N]) resulted of pressure difference (1 [bar]) between the two chambers of the pneumatic cylinder.

The pressures in the two chambers of the pneumatic cylinder are controlled by the two pressure regulating valves separately. The displacement of the cylinder rod

is collected by the displacement sensor with accuracy of 0.03% FS. The force sensors range is 500 kgf and its non-linear error is less than 0.03% FS. The pressure sensor range is 10 bar, with the accuracy of 0.05% FS as mentioned before. All the signals of the sensors are collected by a data acquisition card (DAC) and transferred to the computer. All measurements have been made in real time with sampling time  $t_s = 1$  [ms] with constant supply pressure  $p_s = 10$  [bar], and constant external pressure  $p_{Atm} = 1$  [bar]. The analysis program in the computer helps in treating the measured data and documenting the results. The analysis program calculates the friction force  $F_f$  using the experiment data by applying Newton's second law on the bundle of the piston and its accessories of mass  $M$  as follows:

$$F_f = S(p_1 - p_2) - F_L - Ma \quad (19)$$

where  $S$  is the effective piston area,  $a$  is the acceleration of the piston and its accessories,  $F_L$  is the load force caused by closed hydraulic circuit and measured by the force sensor. Beside  $p_1$ , and  $p_2$  are the pneumatic pressures in the two cylinder chambers as is shown in Figure 15.

**Remark 3.** The velocity and the acceleration have been obtained by the off-line derivation of the position signal using a robust differentiator algorithm: 'adaptive super twist differentiator algorithm' which is given by Dridi (2011) via sliding mode technique, to attenuate the noise related to differentiating process.

#### 4.2.2. Test procedure

By using the setup in Figure 15, each experiment is performed with two different values of pressures  $p_1$ , and  $p_2$  in the two cylinder chambers. Here, two different phases can be distinguished. First phase is the entry phase in which  $p_2 > p_1$  and the piston rod moves to inside the pneumatic cylinder, in this situation, the displacement and the velocity of the piston rod are idiomatically negative. Second phase is the exit phase in which  $p_1 > p_2$  and the piston rod moves to outside the pneumatic cylinder, here, the displacement and the velocity of the piston rod are idiomatically positive. The test procedure in the entry phase (exit phase) is as follows: (1) Put the piston rod of the pneumatic cylinder in the most outer (inner) position. (2) Close the shut-off valve. (3) Adjust the two pressures values  $p_2 > p_1$  ( $p_1 > p_2$ ) in the two pneumatic cylinder chambers. (4) Begin collecting data from the four sensors by the data acquisition card. (5) Open the shut-off valve until the piston rod moves to the most inner (outer) position. (6) End collecting data from the four sensors by the data acquisition card. (7) Save the collected data in a text file on the computer. (8) Repeat the steps 1...7 for the set of values  $I = \{(p_1, p_2): p_1 < p_2, (p_1, p_2) \in [1, 10]^2\}$  in entry phase, and  $O = \{(p_1, p_2): p_1 > p_2, (p_1, p_2) \in [1, 10]^2\}$  in exit phase. Practically, the test procedure in entry phase has been performed for a finite set of twenty-six values

which cover roughly the set  $I$  as follows ( $p_1$  and  $p_2$  in bars):

$$(p_1, p_2) \in \{(1, 9.92), (2.22, 9.9), (4.15, 9.92), (7.18, 9.9), (1, 9.15), (1, 6.93), (1, 5.04), (1, 3.96), (1, 1.65), (2.2, 8.87), (4.23, 8.89), (6.15, 8.88), (8.01, 8.94), (3.21, 7.89), (5.16, 7.85), (7.02, 7.9), (2.22, 6.87), (4.17, 6.88), (5.98, 7.05), (3.02, 5.89), (4.98, 6.04), (2.01, 5.07), (4.07, 5.07), (2.99, 4.2), (1.98, 3.2), (8.54, 10.08)\} \text{ [bar]}$$

The data of sensors resulting from the previous twenty-six experiments have been saved in the computer for the identification of friction parameters as detailed in the next section.

#### 4.2.3. Parameter identification method

The parameters of the static friction model are obtained from the analysis of the experiments data that have been carried out according to the test procedure detailed in the previous section. The Parameter identification method will be repeated for each experiment, and it is sufficient to explain this method for one experiment. So, one of the entry phase experiments, that has been performed with pressure values  $(p_1, p_2) = (1 \text{ [bar]}, 6.93 \text{ [bar]})$  is chosen to apply the method of parameter identification, which is summarised in two essential steps as follows:

**4.2.3.1. Identification of the breakaway force and the stribeck velocity.** By plotting the friction force vs. velocity as shown in Figure 17, the breakaway force and the stribeck velocity cannot be deduced accurately from the stribeck effect region. So, the diagram of the friction force vs. time and the diagram of velocity vs. time must be drawn on the same time scale as shown in Figure 16. By comparing the two diagrams, it is clear that the stribeck effect, which is the decreasing of friction force with an increasing of velocity until the so-called Stribeck velocity  $v_s$  as explained by Virgala and Kelemen (2013), has appeared between the two points of time 1 [ms] and 4 [ms]. Thus, the breakaway force is  $F_s = -95.16$  [N] at the point 1 [ms], and the stribeck velocity at the point 4 [ms] can be directly read from the velocity vs. time diagram at the point 4 [ms]. As result,  $v_s = -0.015$  [m/s]

#### 4.2.3.2. Identification of the viscosity factor and the Coulomb friction.

The experimental data of the friction force vs. the velocity outside the stribeck zone must be depicted as shown in Figure 17. By fitting this data with a Straight line, the inclination of this line represents the viscosity factor  $F_v$ , and the intersection of this line with the friction force axis represents the Coulomb friction  $F_C$ . In this example, the fitting line equation is  $3470 v - 55$ . Thus,  $F_v = 3470$  [Ns/m] and  $F_C = -55$  [N].

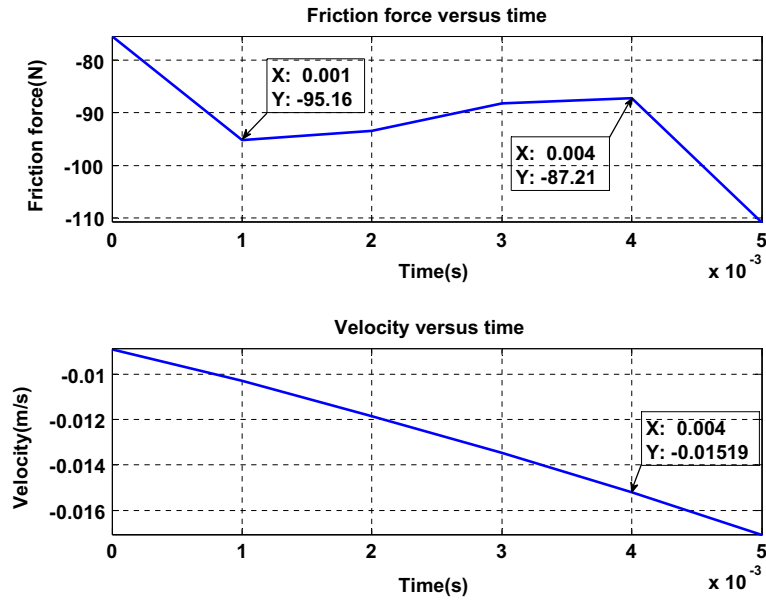


Figure 16. The friction force and velocity near the breakaway point for  $(p_1, p_2) = (1 \text{ [bar]}, 6.93 \text{ [bar]})$ .

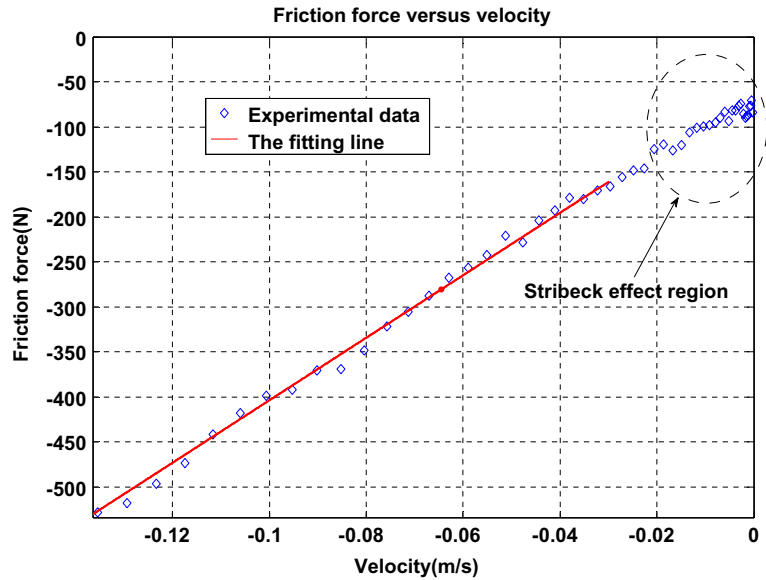


Figure 17. The experimental data of the velocity vs. friction force and the fitting line for  $(p_1, p_2) = (1 \text{ [bar]}, 6.93 \text{ [bar]})$ .

The application of the previous method on the twenty-six experiments in the entry phase gives the four parameters of the static friction model in the twenty-six states of the pressures in the two cylinder chambers. In other words, the four parameters of static friction model are given as a function of the pressures in the two cylinder chambers. The fitting surface of each parameter is a plane with a maximum relative error less than 5%. The equations of the planes have been identified as in Equations (20)–(23), that are depicted in Figures 18–21, respectively.

$$F_{S_{en}}(p_1, p_2) = -27.31 + 12.95 p_1 - 11.6 p_2 \quad [\text{N}] \quad (20)$$

$$v_{S_{en}}(p_1, p_2) = -0.00752 + 0.00097 p_1 - 0.00122 p_2 \quad [\text{m/s}] \quad (21)$$

$$F_{v_{en}}(p_1, p_2) = 53.8 + 265.2 p_1 + 450 p_2 \quad [\text{Ns/m}] \quad (22)$$

$$F_{C_{en}}(p_1, p_2) = -15.52 + 8.413 p_1 - 7.028 p_2 \quad [\text{N}] \quad (23)$$

The parameter identification of the static friction model in exit phase is accomplished in the same way as the entry phase, but with a less number of trials, taking advantage of the fact that the surfaces which represent the parameters of the static friction model in exit phase are planes as in the entry phase, and the fact that the plane is determined by two intersecting lines, so the experiments of set O which lie on two intersecting lines in the plane  $(p_1, p_2)$  are sufficient to identify the parameters of the static friction model in exit phase. Practically, the test procedure in exit phase has been performed for

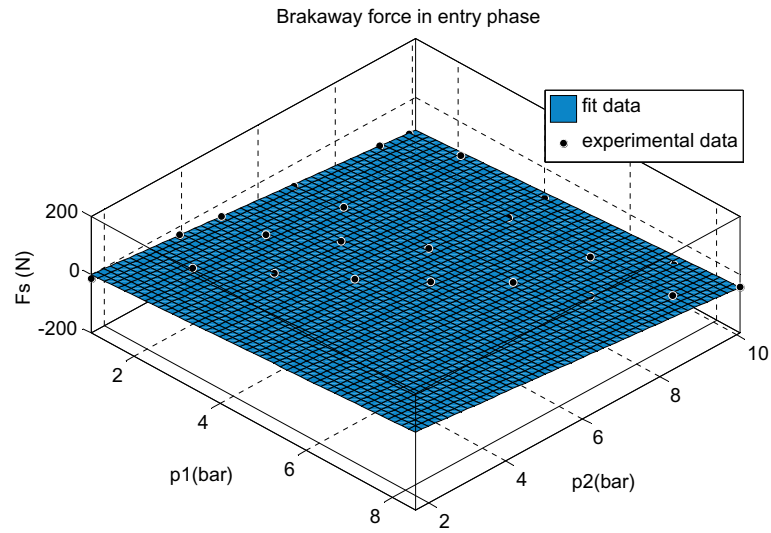


**Figure 18.** The brakeway force as a function of the pressure in the two cylinder chambers in the entry phase.

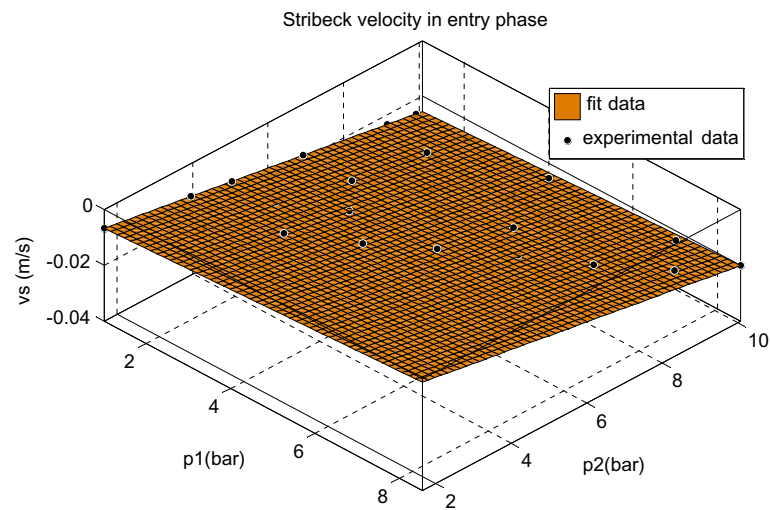


**Figure 19.** The stribeck velocity as a function of the pressure in the two cylinder chambers in the entry phase.

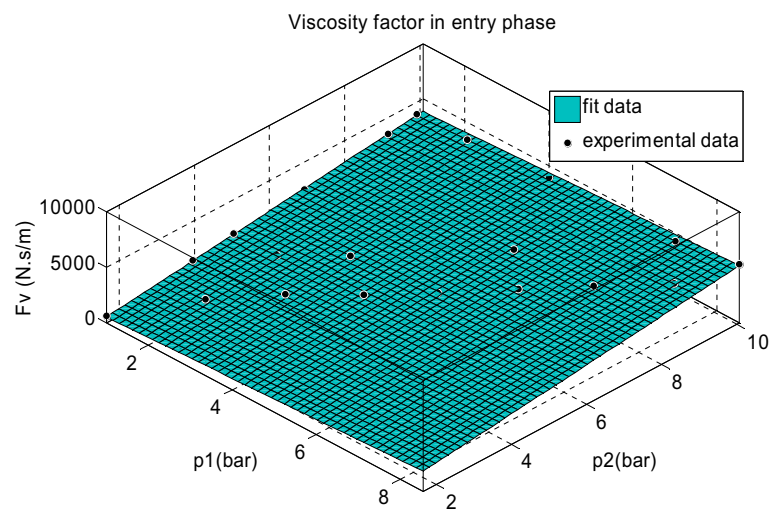


**Figure 20.** The viscosity factor as a function of the pressure in the two cylinder chambers in the entry phase.

a finite set of eleven values of the set  $O$ , which represent nearly a two intersecting lines in the plane  $(p_1, p_2)$ , as follows:

$$(p_1, p_2) \in \{(1.78, 1), (4.015, 1), (4.96, 1), (6.89, 1), (7.97, 1), (8.98, 1), (10.0075, 1), (10.115, 8.89), (10.225, 6.955), (10.205, 4.195), (10.15, 2.105)\} \text{ [bar]}$$

The fitting surface of each parameter of the static friction model in exit phase is a plane with a maximum relative error less than 5%, and the equations of the fitting planes have been identified as in Equations (24)–(27) that are depicted in Figures 22–25, respectively.

$$F_{S_{ex}}(p_1, p_2) = 26.39 + 12.4 p_1 - 14.43 p_2 \text{ [N]} \quad (24)$$

$$v_{S_{ex}}(p_1, p_2) = 0.00928 + 0.00122 p_1 - 0.00097 p_2 \text{ [m/s]} \quad (25)$$

$$F_{v_{ex}}(p_1, p_2) = -407.6 + 325.8 p_1 + 355.6 p_2 \text{ [Ns/m]} \quad (26)$$

$$F_{C_{ex}}(p_1, p_2) = 26.16 + 8.575 p_1 - 11.72 p_2 \text{ [N]} \quad (27)$$

A check test of the friction model has been carried out by applying Newton second law on the bundle of the piston and its accessories as in Equation (19). The check process has been fulfilled taking into account the static friction model  $F_f(v, p_1, p_2)$  which has been obtained previously in the case of no load ( $F_L = 0$ ). The Newton second law can be represented by the block diagram as shown in Figure 26, where  $y, \dot{y}, \ddot{y}$  are the position, the velocity, and the acceleration of cylinder piston, respectively. In the check process, two real ‘pressure maps’ have been applied (by the servo valve) in the two cylinder chambers as depicted in Figure 27, and the real trajectory resulting of these ‘pressure maps’ has been recorded. After that, the computed trajectory resulting of the applying

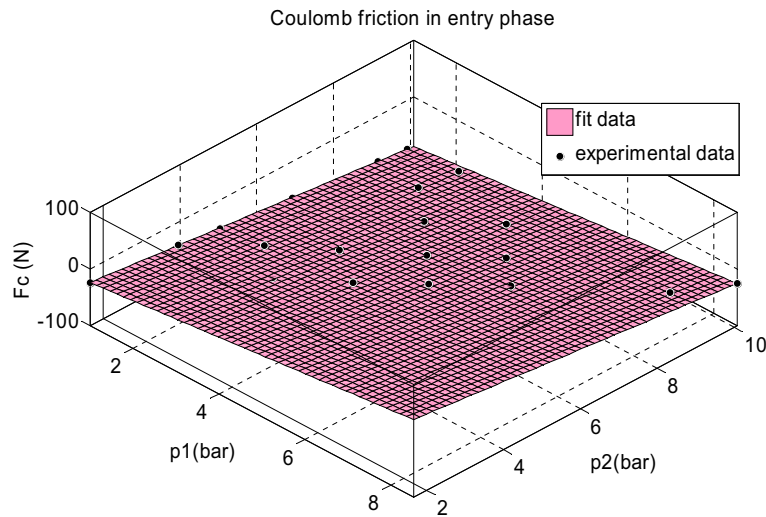


Figure 21. The Coulomb friction as a function of the pressure in the two cylinder chambers in the entry phase.

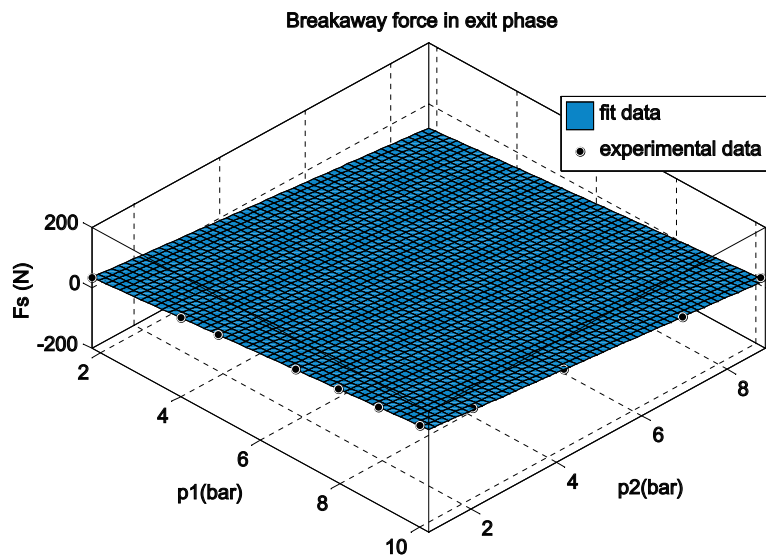
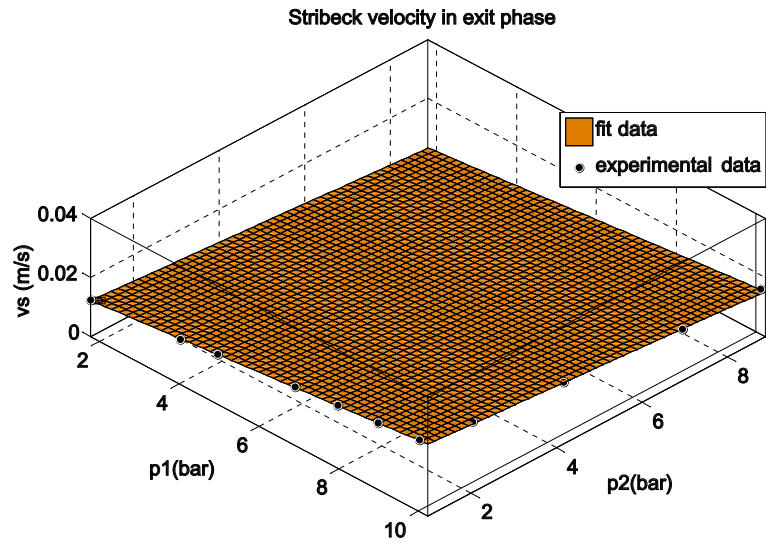
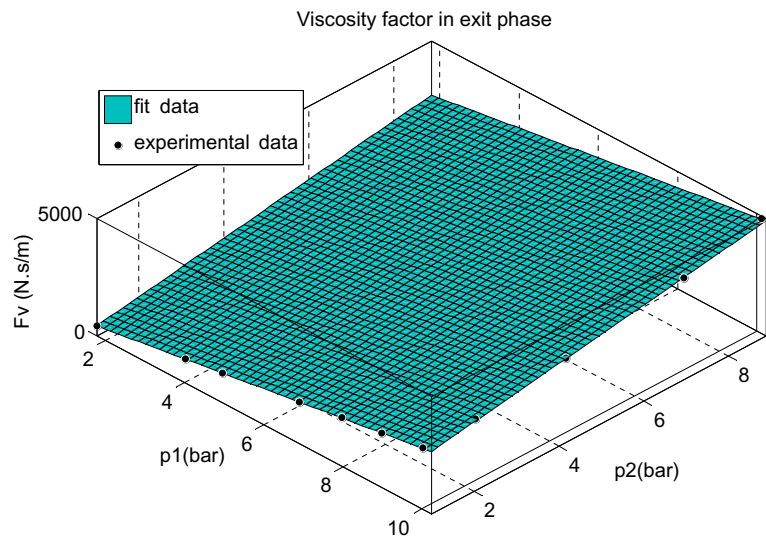


Figure 22. The breakaway force as a function of the pressure in the two cylinder chambers in the exit phase.



**Figure 23.** The stribeck velocity as a function of the pressure in the two cylinder chambers in the exit phase.



**Figure 24.** The viscosity factor as a function of the pressure in the two cylinder chambers in the exit phase.

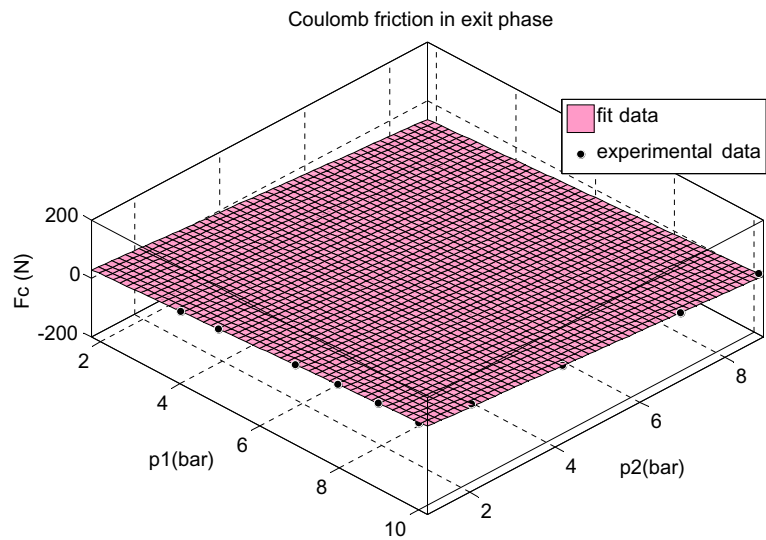


**Figure 25.** The Coulomb friction as a function of the pressure in the two cylinder chambers in the exit phase.

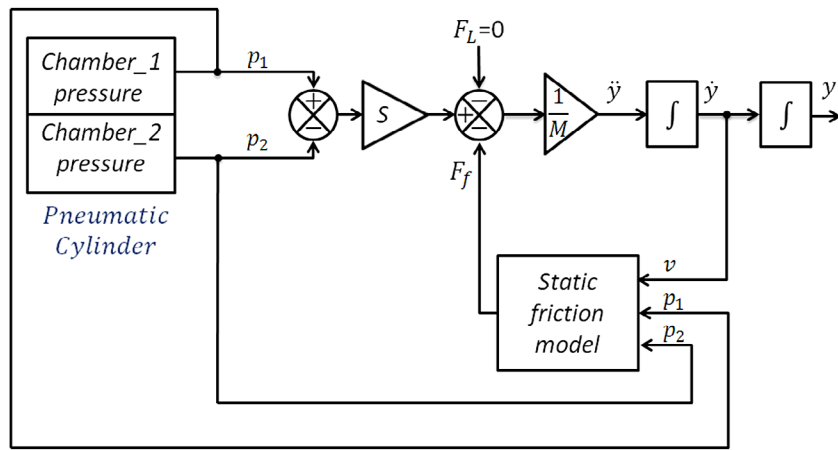


Figure 26. Block diagram represents the Newton second law application on the bundle of the piston and its accessories.

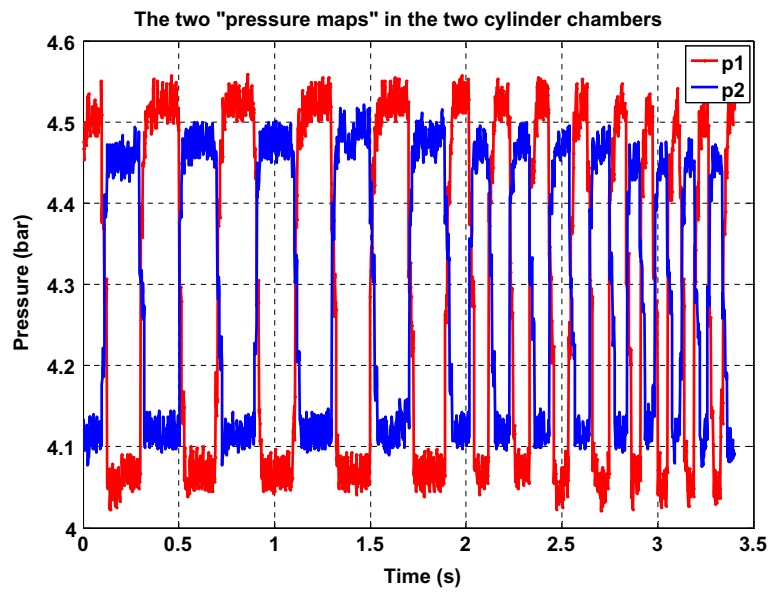


Figure 27. The two 'pressure maps' that applied in the two cylinder chambers.

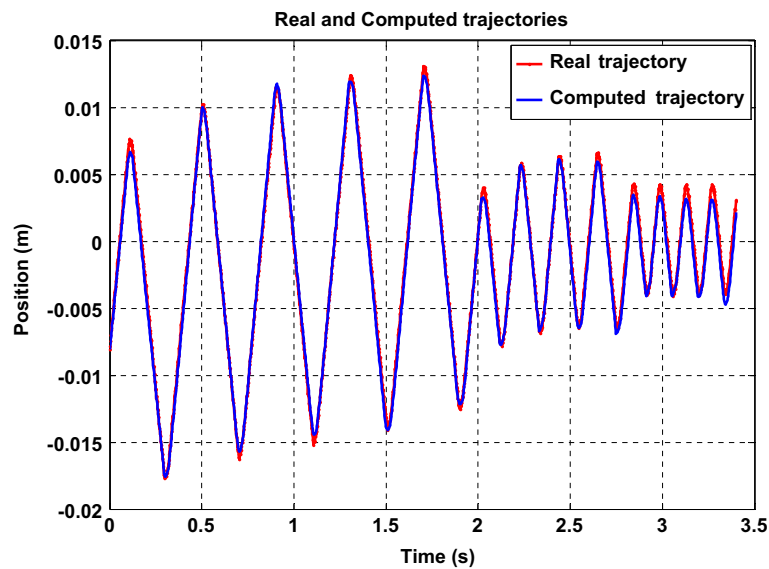


Figure 28. The real and the computed trajectories.

of Newton second law, and the real trajectory have been depicted in Figure 28. By comparing the two trajectories, the computed trajectory and the real trajectory are almost identical. As result, the static friction model  $F_f(v, p_1, p_2)$  can simulate the real case accurately.

### 5. The nonlinear model

The complete nonlinear model can be represented by the block diagram shown in Figure 29. It is the result of assembling the nonlinear model of the jet pipe electro-pneumatic servo valve, the rate of change of the

pressure inside each chamber of the pneumatic cylinder, and the mechanical equations applied to the piston and its accessories including the friction force model.

### 6. Experimental validation of the nonlinear model

The nonlinear model of the jet pipe electro-pneumatic servo actuator must be validated in the frequency and time domains. So, a validation process has been performed by comparing the frequency and time responses of the nonlinear model with the measured frequency and

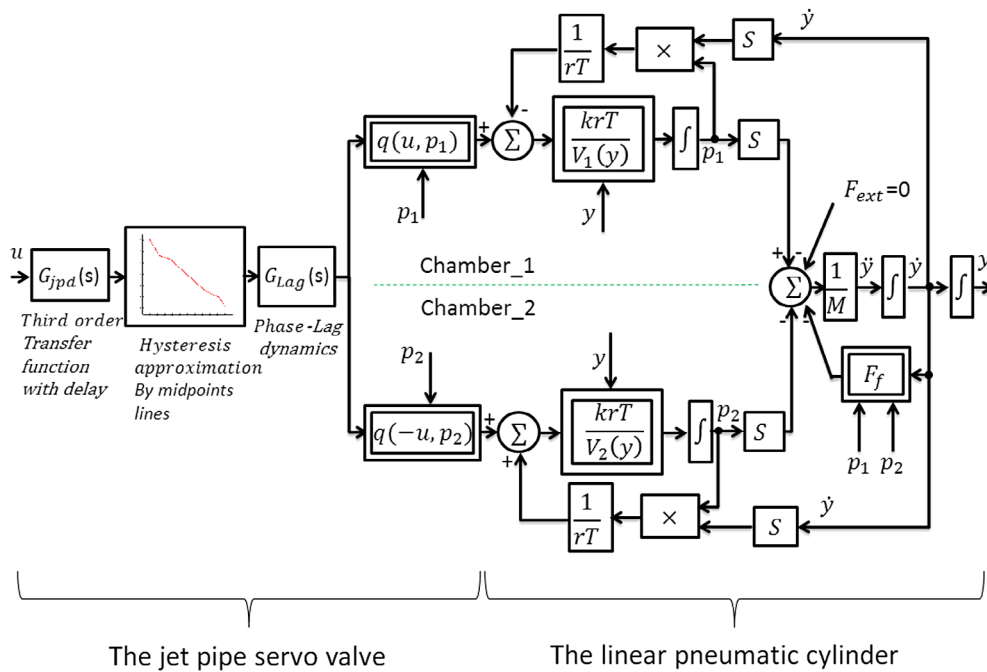


Figure 29. The nonlinear model of the jet pipe electro-pneumatic servo actuator.

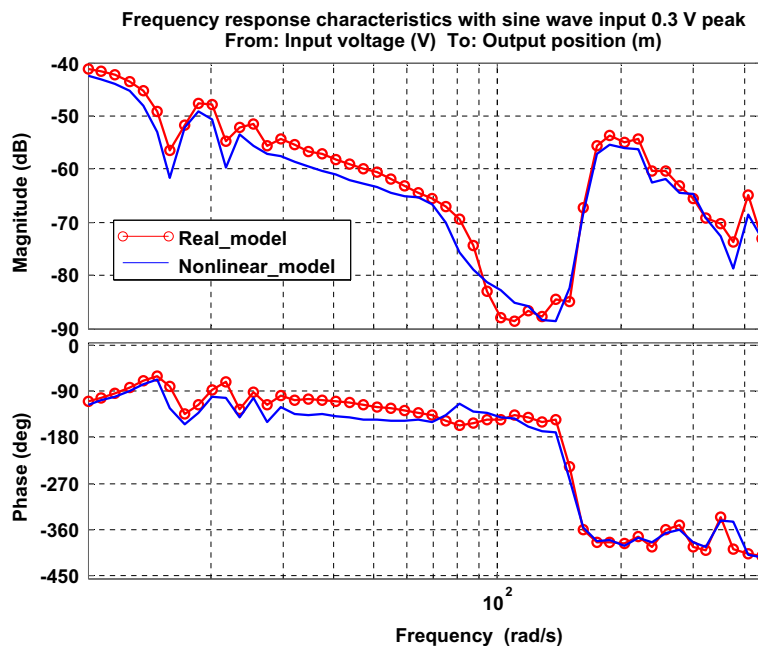


Figure 30. The frequency responses characteristics of the nonlinear model and the real system to input 0.3 [V] peak.

measured time responses of the jet pipe electro-pneumatic servo actuator (the real system) with the same input signals. Here, the intended frequency and time responses relates the input voltage in [V] to the output position in [m]. In frequency response, the jet pipe electro-pneumatic servo actuator is fed by a flow of compressed air with constant supply pressure  $p_s = 10$  [bar] and forced to move periodically by input sine wave with frequency range (1.6–70 [Hz]). All measurements of input and output signal have been made in real time with sampling time  $t_s = 1$  [ms].

The frequency responses characteristics of the nonlinear model and the real system to a sine wave input 0.3 [V] peak, and 1.5 [V] peak are shown in Figures 30 and 31, respectively. The time responses characteristics

of the nonlinear model and the real system to a square wave input (0.6 [V] peak, 0.1122 [Hz]) and (3 [V] peak, 0.97 [Hz]) are shown in Figures 32 and 34, respectively. The error between nonlinear model and real system in time responses characteristics are shown in Figures 33 and 35. The frequency responses characteristics of the nonlinear model and the real system are close in frequency range (1.6–70 [Hz]) for small and big amplitude. Time responses characteristics of the nonlinear model and the real system to square input signal are close for small and big amplitudes. Finally, the validation process confirms that the nonlinear model represents the real system with acceptable error (less than 12% in gain response, less than 12% in phase response and less than 12% in position time response). This error is due

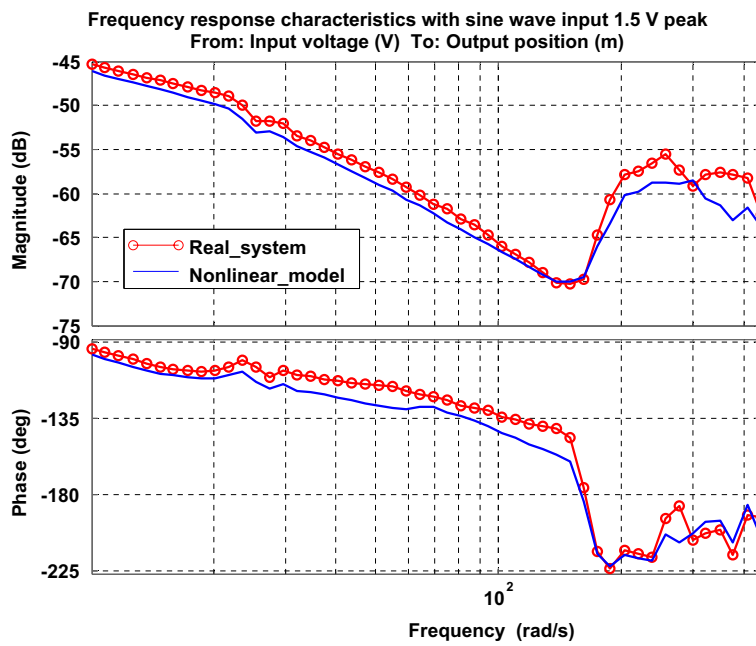


Figure 31. The frequency responses characteristics of the nonlinear model and the real system to input 1.5 [V] peak.

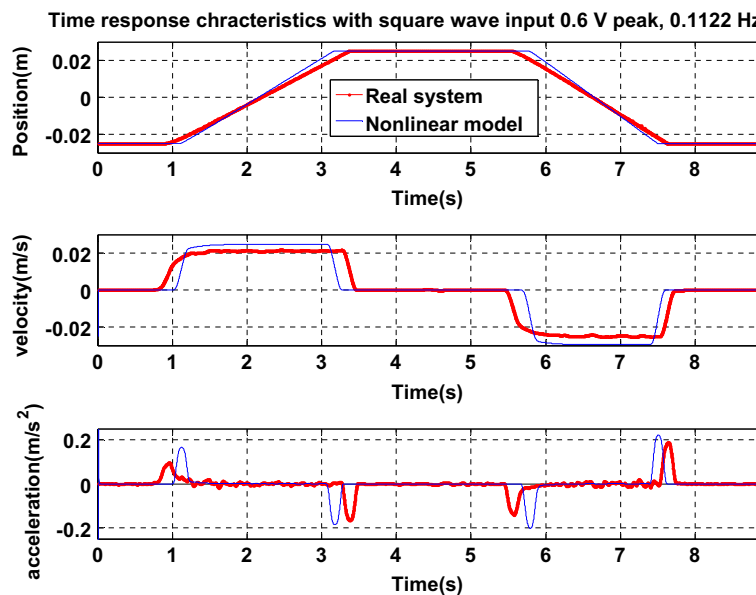
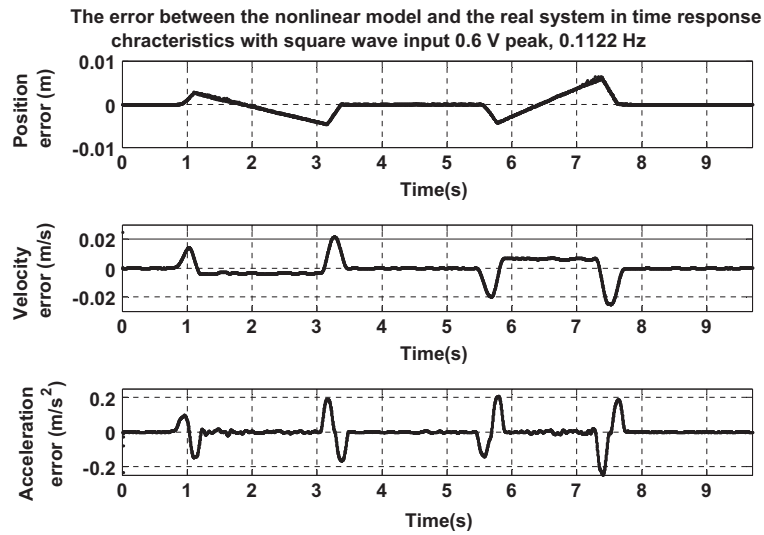
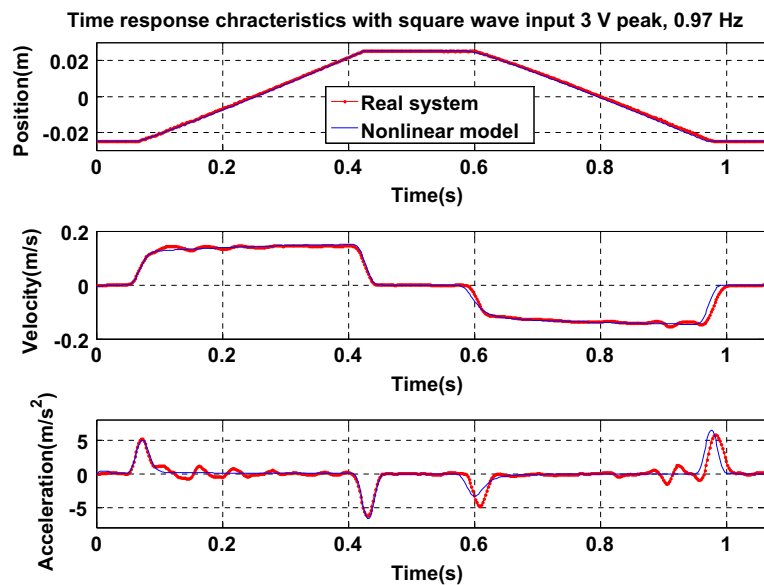


Figure 32. Time responses of nonlinear model and real system to square wave input 0.6 [V] peak, 0.1122 [Hz].



**Figure 33.** The error between nonlinear model and real system in time responses characteristics with square wave input 0.6 [V] peak, 0.1122 [Hz].



**Figure 34.** Time responses of nonlinear model and real system to square wave input 3 [V] peak, 0.97 [Hz].

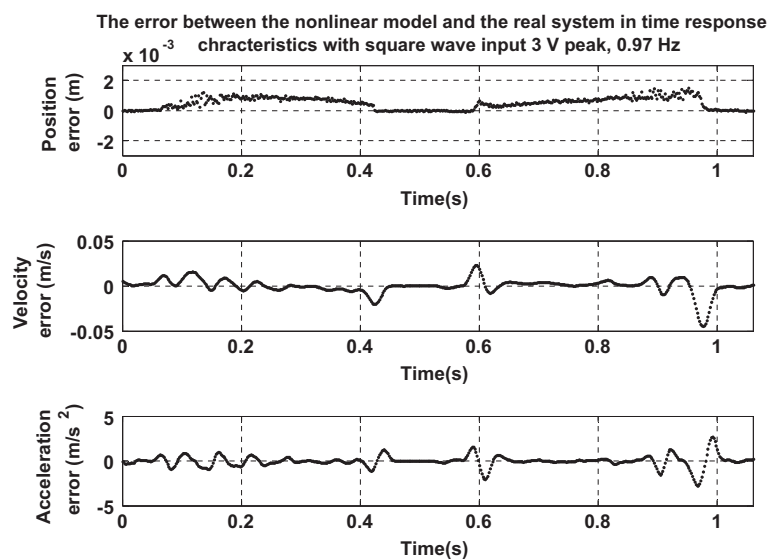


**Figure 35.** The error between the nonlinear model and the real system in time responses characteristics with square wave input 3 [V] peak, 0.97 [Hz].

to the servo valve modelling error, friction modelling error, and the non-modelled phenomena as the friction dynamics.

## 7. Conclusions

This paper presents a general procedure of parameter identification for a jet pipe electro-pneumatic servo actuator; however the derived model is only valid for the exact set up of the chosen actuator. A nonlinear model of the jet pipe electro-pneumatic servo valve has been built and validated. The Gaussian exponential static friction model, which can describe the friction phenomena of actuator cylinder in sliding regime as a function of the piston relative velocity and the pressures in the two cylinder chambers, has been identified and checked. Subsequently, the final nonlinear model of the jet pipe electro-pneumatic servo actuator has been built by assembling the nonlinear model of the jet pipe electro-pneumatic servo valve, the model of the two cylinder chambers represented by the rate of change of the pressure inside each chamber, and Newton's second law applied to the piston and its accessories including the static friction model. Finally, a validation process has been performed by comparing the frequency and time responses of the nonlinear model with that of the real system. The validation process has shown that the nonlinear model can represent the real system with an acceptable error (less than 12% in gain response, less than 12% in phase response and less than 12% in position time response) which is due to servo valve modelling error, friction modelling error, and the non-modelled phenomena as the friction dynamics. The main drawback in this modelling is that the complexity of the non-linear model causes a difficulty in the controller design. To overcome this problem, the fast dynamic of the servo valve represented by the third order transfer function with lag behaviour can be neglected vs. the slow dynamic of the servo actuator and the nonlinear model of the mass flow rate can be converted to a nonlinear affine model with control signal, then nonlinear control techniques can be applied to design the appropriate controllers.

## Disclosure statement

No potential conflict of interest was reported by the authors.

## Notes on contributors



**Shawki Al-Saloum** was born in Homs, Syria, in 1974. He received the BS degree in mechanical engineering from HIAST (Higher Institute for Applied sciences and Technologies), Damascus, Syria, in 1998 and the MS degree in control engineering, in 2010. He is currently pursuing the PhD degree in control engineering in HIAST.

From 1999 to 2007, he was a technical engineer in HIAST. From 2010 to 2013, he was a Researcher Assistant in control projects in HIAST.



**Ali Taha** was born in Damascus, Syria, in 1967. He received the BS degree in mechanical engineering from Damascus University, Damascus, Syria, in 1990, and received the MS degree in electro-hydraulic systems from Hua Zong University of technology, Wuhan, China, in 2000, and the PhD degree in control of electro-hydraulic systems from Bauman University of technology, Moscow, Russia in 2007. From 2007 till now, he is a Researcher in HIAST.



**Ibrahim Chouaib** was born in Damascus, Syria, in 1966. He received the BS degree in aeronautic engineering from ENSICA (Ecole Nationale Supérieure d'Ingenieurs du Construction Aéronautiques), Toulouse, France and received the DEA (Diplôme d'étude Approfondi) and the PhD degree in automatic control from INSA (Institute National de Science Appliqués), Toulouse, France, in 1994. From 1995 to 2011, he was a Researcher in HIAST, Damascus, Syria. From 2001 till 2011, he was a principle Researcher in HIAST. From 2011 till now, he is a senior Researcher in HIAST.

## ORCID

Ali Taha  <http://orcid.org/0000-0002-7935-6557>

Ibrahim Chouaib  <http://orcid.org/0000-0003-0997-8876>

## References

- Ali, H.I., *et al.*, 2009. Mathematical and intelligent modeling of electropneumatic servo actuator systems. *Australian journal of basic and applied sciences*, 3 (4), 3662–3670.
- Brun, X., 1999. *Commandes linéaires et non linéaires en électropneumatique. Méthodologies et Applications* [Linear and nonlinear controls in electropneumatic. Methodologies and application]. Doctoral dissertation. INSA Lyon. (In French).
- De Wit, C.C., *et al.*, 1995. A new model for control of systems with friction. *IEEE transactions on automatic control*, 40 (3), 419–425.
- Dridi, M., 2011. *Dérivation numérique: synthèse, application et intégration* [Numerical differentiation: Synthesis, application and integration]. Doctoral dissertation. Ecole Centrale de Lyon. (In French).
- Girin, A., 2007. *Contribution à la commande non linéaire d'un système électropneumatique pour une utilisation aéronautique: application sur un benchmark dédié* [Contribution to nonlinear control of electro-pneumatic system with a new test bench for aeronautics application]. Doctoral dissertation. Ecole Centrale de Nantes (ECN). (In French).
- Heipl, O. and Murrenhoff, H., 2011. Rate- and state-dependent friction model for elastomeric seals. *Proceedings of the 8th JFPS international symposium on fluid power*, 1C3-2, 248–253.
- Henri, P.D., Hollerbach, J.M., and Nahvi, A., 1998. An analytical and experimental investigation of a jet pipe controlled electropneumatic actuator. *IEEE transactions on robotics and automation*, 14 (4), 601–611.

- Le, M.Q., 2011. *Development of bilateral control for pneumatic actuated teleoperation system*. Doctoral dissertation. INSA de Lyon.
- Serafin, S., 2004. *The sound of friction: real-time models, playability and musical applications*. Doctoral dissertation. Stanford university.
- Thorncroft, G., 2007. *Modeling compressible air flow in a charging or discharging vessel and assessment of polytropic exponent*. San Luis Obispo, CA: California Polytechnic.
- Tijani Ismaila, B., Salami, M.J.E., and Akmeliawati, R., 2011. Artificial intelligent based friction modelling and compensation in motion control system. *In: Horacio Martinez Alfaro ed., Advances in mechatronics*. Kuala Lumpur: InTech, 43–68. ISBN: 978-953-307-373-6.
- Toorani, F., Farahmandzad, H. and Aghamirsalim, M., 2010. Gray-box modeling of a pneumatic servo-valve. *Acta polytechnica hungarica*, 7 (5), 129–142.
- Valdiero, A.C., et al., 2011. Nonlinear mathematical modeling in pneumatic servo position applications. *Mathematical problems in engineering*, 2011. Article ID 472903, 16 p. doi: <http://dx.doi.org/10.1155/2011/472903>.
- Virgala, I. and Kelemen, M., 2013. Experimental friction identification of a DC motor. *International journal of mechanics and applications*, 3 (1), 26–30.